

# RadMamba: Efficient Human Activity Recognition through a Radar-based Micro-Doppler-Oriented Mamba State-Space Model

Yizhuo Wu<sup>✉</sup>, *Student Member, IEEE*, Francesco Fioranelli<sup>✉</sup>, *Senior Member, IEEE*  
Chang Gao<sup>\*✉</sup>, *Member, IEEE*

**Abstract**—Radar-based Human Activity Recognition (HAR) is an attractive alternative to wearables and cameras because it preserves privacy, and is contactless and robust to occlusions. However, dominant Convolutional Neural Network (CNN)- and Recurrent Neural Network (RNN)-based solutions are computationally intensive at deployment, and recent lightweight Vision Transformer (ViT) and State Space Model (SSM) variants still exhibit substantial complexity. In this paper, we present *RadMamba*, a parameter-efficient, micro-Doppler-oriented Mamba SSM tailored to radar HAR under on-sensor compute, latency, and energy constraints typical of distributed radar systems. RadMamba combines (i) channel fusion with downsampling, (ii) Doppler-aligned segmentation that preserves the physical continuity of Doppler over time, and (iii) convolutional token projections that better capture Doppler-span variations, thereby retaining temporal-Doppler structure while reducing the number of Floating-point Operations/Inference (#FLOP/Inf.). Evaluated across three datasets with different radars and types of activities, RadMamba matches the prior best 99.8% accuracy of a recent SSM-based model on the Continuous Wave (CW) radar dataset, while requiring only 1/400 of its parameters. On a dataset of non-continuous activities with Frequency Modulated Continuous Wave (FMCW) radar, RadMamba remains competitive with leading 92.0% results using about 1/10 of the parameters, and on a continuous FMCW radar dataset it surpasses methods with far more parameters by at least 3%, using only 6.7 k parameters. **Code:** <https://github.com/lab-emi/AIRHAR>.

**Index Terms**—Human activity recognition, Mamba state-space model, FMCW radar, micro-Doppler signatures, deep learning, parameter-efficient networks, continuous monitoring, radar signal processing

## I. INTRODUCTION

HUMAN Activity Recognition (HAR) technologies are central to healthcare, elderly care, smart homes, and security. Traditional HAR solutions rely on wearable sensors or cameras. While wearables can offer precise monitoring, they suffer from issues related to user compliance, battery life, and comfort. Camera-based approaches raise privacy concerns and are at high risk of degradation under challenging environmental conditions. Consequently, Radar-based Human Activity Recognition (RadHAR) has emerged as a compelling alternative, leveraging active electromagnetic sensing to infer behaviors while preserving privacy, maintaining robustness to illumination and occlusions, and enabling through-wall sensing [1], [2].

Yizhuo Wu, Francesco Fioranelli, and Chang Gao are with the Department of Microelectronics, Delft University of Technology, The Netherlands.

\*Corresponding author: Chang Gao (chang.gao@tudelft.nl)

Early RadHAR studies progressed from simple, isolated activities [3], [4] to more realistic settings involving continuous activity monitoring [5], [6], multi-modal and distributed sensing [7], [8], and advanced classifiers. Conventional machine learning with hand-crafted micro-Doppler features (e.g., centroid, bandwidth, statistical descriptors, and Singular Value Decomposition (SVD) components) [4]–[6], [9] demonstrated proof of concept but struggled with scalability and generalization in continuous scenarios.

Deep learning improved accuracy by learning spatio-temporal representations directly from radar signatures. CNN-based methods [10]–[13], RNN-based methods [7], [14], and hybrid CNN-RNN models [15]–[17] substantially advanced performance. However, they often have high computational cost and latency, which limits on-sensor deployment in resource-constrained radar nodes. More recently, transformer and SSM-based architectures [18]–[23] have shown strong modeling capacity and explored lightweight designs, but balancing parameter count with computational efficiency, measured by the number of floating-point operations per inference (#FLOP/Inf.), remains challenging for mobile and distributed applications such as gesture interfaces [24] and smart-home radar networks [8].

Micro-Doppler signatures encode the evolution of Doppler frequency over time. Preserving this physical continuity is crucial for maintaining the high accuracy of sequential models; however, common vision-style rectangular patching and tokenization can disrupt Doppler-time ordering and waste computational resources on sparse, low-information regions. Moreover, edge radar deployments impose strict limits on memory, latency, and energy per inference. These constraints motivate architectures that (i) respect the physical features of radar signatures and sparsity patterns and (ii) reduce arithmetic intensity without sacrificing discriminative Doppler structure.

In this work, we propose RadMamba, a radar-oriented, parameter-efficient Mamba SSM for micro-Doppler classification. RadMamba replaces vision-style patching and purely linear token projections with three radar-driven mechanisms: (i) *channel fusion with downsampling* to mix channels and shrink low-information regions; (ii) *Doppler-aligned segmentation* that preserves Doppler-time continuity for state-space modeling; and (iii) *convolutional token projections* to capture Doppler-span variations better and improve inter-patch coherence for the SSM backbone.

The main contributions of this work are:

- A radar-centric state-space architecture that preserves the physical structure of micro-Doppler signatures via Doppler-aligned segmentation and convolutional token projections, reducing #FLOP/Inf. while maintaining temporal-Doppler fidelity.
- A comprehensive evaluation across CW and FMCW datasets covering non-continuous and continuous settings: RadMamba attains 99.8% on a dataset measured by the Defence Institute of Advanced categorization problems and classification Technology, India (DIAT) [25], 91.2% on a dataset from the laboratory of Computational Intelligence for Radar (CI4R) [26] (competitive with heavier models), and 89.3% on a dataset collected at the University of Glasgow in 2020 (UoG20) [27] (at least 3% higher than prior methods with far more parameters), with substantially fewer parameters and lower #FLOP/Inf. across all three datasets.
- An ablation study showing the synergistic effect of (i) channel fusion with downsampling, (ii) Doppler-aligned segmentation, and (iii) convolutional projections, each contributing to efficiency and accuracy beyond conventional ViT/SSM patching and linear projections.
- An open-source PyTorch framework, RadHAR, to facilitate reproducible research and rapid prototyping for micro-Doppler HAR.

## II. RELATED WORKS

### A. Conventional machine learning method

These methods involved extracting domain-specific features from radar signals, followed by classification using algorithms like k-Nearest Neighbors (kNN) and Support Vector Machine (SVM). For instance, Erol et al. [5] used kNN to analyze power burst curves in spectrograms for fall detection, distinguishing fall from non-fall events. Li et al. [6] applied SVMs to micro-Doppler features such as Doppler centroid, bandwidth, and SVD components, while Ding et al. [9] extracted 28 features of four types: dynamic Doppler frequency, range change, energy change, and dispersion of range and Doppler from dynamic range-Doppler trajectories for subspace kNN classification. Although effective in controlled environments, these approaches struggled to generalize across diverse conditions and activities due to their dependence on hand-crafted features, often leading to overfitting and poor scalability for continuous tasks [1], [2].

### B. CNN-based method

The shift to deep learning marked a turning point for RadHAR, with CNNs leading the charge. Unlike traditional methods, CNNs automatically learn spatial hierarchies from radar representations like spectrograms and range-Doppler maps. Kang et al. [28] employed CNNs in a two-step process for segmenting and classifying activity sequences, achieving over 97% segmentation accuracy and 95% classification accuracy with 60 GHz millimeter-wave radar data. Yu et al. [13] introduced a ‘Dual-View CNN’ operating on orthogonal projections of voxelized point clouds, reaching 97.61% accuracy.

However, when CNNs are applied only to micro-Doppler maps treated as images, they lack inherent temporal modeling, which is a critical limitation for continuous activity recognition.

### C. RNN-based method

To address temporal dynamics in human activities, researchers have incorporated RNNs, particularly Long Short-Term Memory (LSTM) [29] and Gated Recurrent Unit (GRU) [30] networks, which are specifically designed for sequential data processing. Shrestha et al. [27] demonstrated the superiority of bidirectional LSTM networks over traditional SVMs and standard LSTMs in continuous activity recognition. Werthen-Brabants et al. [14] proposed an innovative split Bidirectional (Bi)-RNN architecture for real-time fall alerts, using separate forward & backward RNN components for immediate, refined predictions.

### D. Hybrid CNN-RNN-based method

Recognizing the complementary strengths of CNNs and RNNs, hybrid architectures emerged as a dominant paradigm. These models typically combine CNN-based spatial feature extraction with RNN-based temporal modeling. Kurtoglu et al. [15] implemented a sophisticated multi-modal approach, utilizing 3D CNNs with Bi-LSTM layers for range-Doppler maps and 2D/1D CNNs with Bi-LSTM for spectrograms and envelopes, achieving 93.3% accuracy for continuous activities mixed with American Sign Language [31]. Zhu et al. [16] integrated CNN-extracted features with LSTM-based temporal modeling, achieving 98.65% accuracy on a non-continuous Doppler radar human activity recognition task with 7 classes.

For distributed radar systems, hybrid models achieve an accuracy of 87.1% in continuous activity recognition tasks with only 71 k parameters [17]. Compared to CNN-based models in non-continuous tasks that utilize 135 M parameters [32] and RNN-based models in continuous tasks that utilize 189 M parameters [27] to achieve their best classification accuracy, hybrid models are more lightweight. However, the #FLOP/Inf. required by the hybrid model [17] is evaluated to be at least 1 G. The arithmetic intensity of CNNs, especially for multi-channel signals, drives their computational complexity.

### E. Transformer and SSM-based method

Recently, researchers have explored transformer-based architectures and SSM in RadHAR. ViT-based methods [19] achieved 92% accuracy with 2.7 M parameters, while [33] reached 92.1% with 769 k parameters on non-continuous FMCW radar data [25], though both demand significant #FLOP per inference. (169 M and 2.41 G, respectively). In continuous HAR, however, ViT appears to underperform conventional CNN-based models, such as the first three blocks of AlexNet and ResNet [20]. SSM-based approaches [22] hit 99.82% accuracy on a non-continuous CW dataset [25] with 8.7 M parameters and 1.22G #FLOP per inference. Compared to ultra-lightweight object detection models optimized for edge devices, such as YOLO-Fastest with 350 k parameters, and 252 M #FLOP/Inf, directly applying these advanced architectures to radar-based HAR tasks remains costly due to their high computational overhead.

### Proposed RadMamba Schematic

■ New Approaches in RadMamba

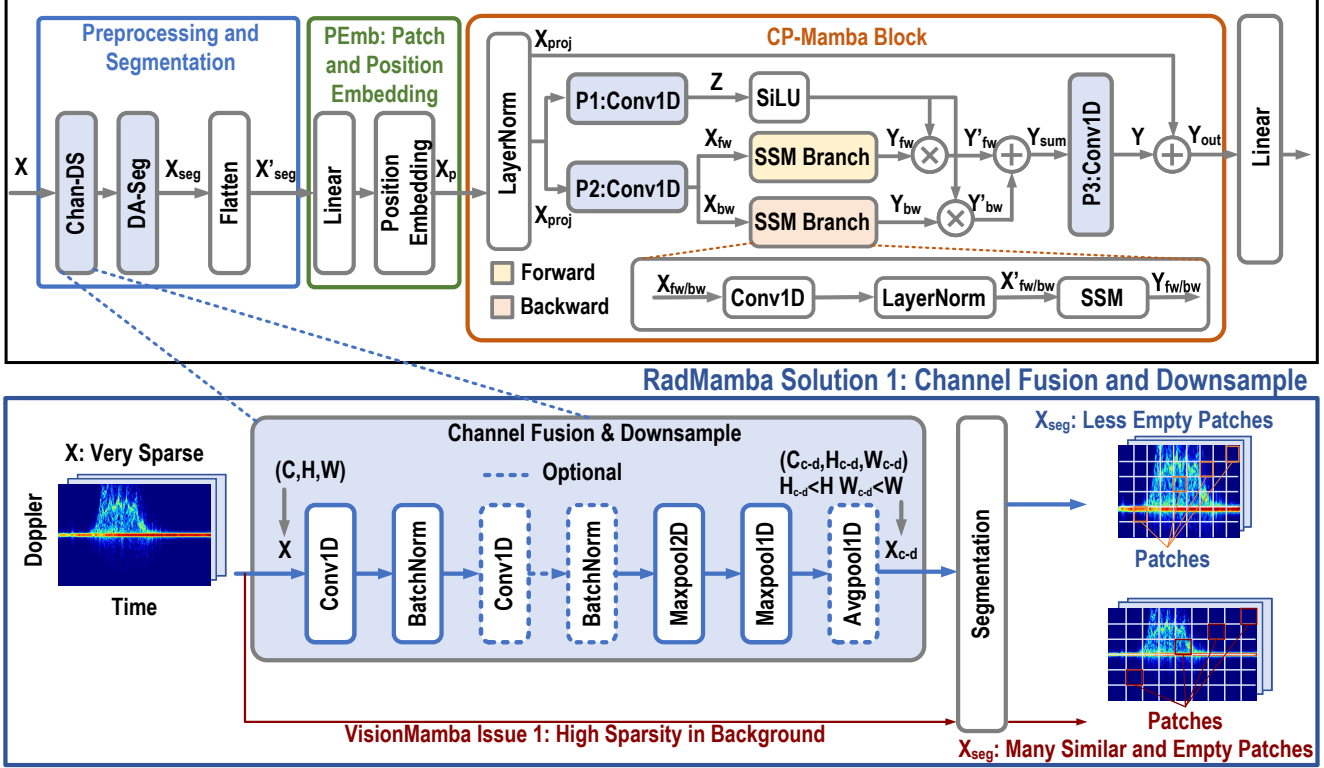


Fig. 1. The schematic of the proposed RadMamba architecture and its novel Solution 1 for radar micro-Doppler-based classification.

### III. PROPOSED RADMAMBA

To effectively combine the modeling power of SSM with lower computational cost, it is essential to exploit the distinctive characteristics of micro-Doppler signatures. However, applying a conventional Vision Mamba (ViM) to RadHAR reveals three key issues:

- **Issue 1:** Micro-Doppler signatures exhibit significant background sparsity, so most time-frequency bins carry little task-relevant information.
- **Issue 2:** Rectangular patch segmentation disrupts the continuous spatio-temporal structure of micro-Doppler patterns, degrading representation quality.
- **Issue 3:** Standard linear projection layers struggle to capture Doppler-specific, time-frequency patterns.

To clarify these points, we trace the data flow from input to SSM in RadMamba, highlighting issues specific to radar micro-Doppler-based HAR tasks and describing our proposed solutions in RadMamba. As shown in Fig. 1, RadMamba consists of three core components: preprocessing and segmentation; patch and positional embedding; and a convolution-projection-based Mamba block with bidirectional SSMs. We customize the architecture for micro-Doppler signals using three solutions: channel fusion with downsampling, Doppler-aligned segmentation, and the Convolutional Projection-based Mamba (CP-Mamba) block.

#### A. Solution 1: Channel Fusion and Downsampling

The micro-Doppler signature  $\mathbf{X} \in \mathbb{R}^{C \times H \times W}$  serves as input to the classifier, with the Doppler frequency dimension represented as the image height  $H$  and time as the image width  $W$ . The channel dimension  $C$  corresponds either to multiple radar signal channels or to RGB channels when visualized as an image. In the subsequent *Segment* step,  $\mathbf{X}$  is partitioned into a matrix of smaller patches, denoted as  $\mathbf{X}_{seg}$ . As depicted in Fig. 1 VisionMamba Issue 1, many patches in  $\mathbf{X}_{seg}$  contain only background information and therefore appear visually redundant. Based on our analysis of the CI4R Dataset [26], the micro-Doppler spectrograms exhibit an average spectrogram sparsity of approximately 87%. Such sparse background regions contribute limited discriminative information regarding Doppler frequency or temporal dynamics, reducing the representational effectiveness of these patches.

To address the high sparsity inherent in micro-Doppler signatures, we introduce a preprocessing pipeline, Channel Fusion and Downsampling (Chan-DS), before the segmentation stage, as depicted in Fig. 1.

$$\mathbf{X}_{c-d} = \text{Chan-DS}(\mathbf{X}) \quad (1)$$

where  $\mathbf{X}_{c-d} \in \mathbb{R}^{C_{c-d} \times H_{c-d} \times W_{c-d}}$  with  $H_{c-d} < H$  and  $W_{c-d} < W$  is the micro-Doppler signature after channel fusion and downsampling. The architecture of the *Chan-DS*

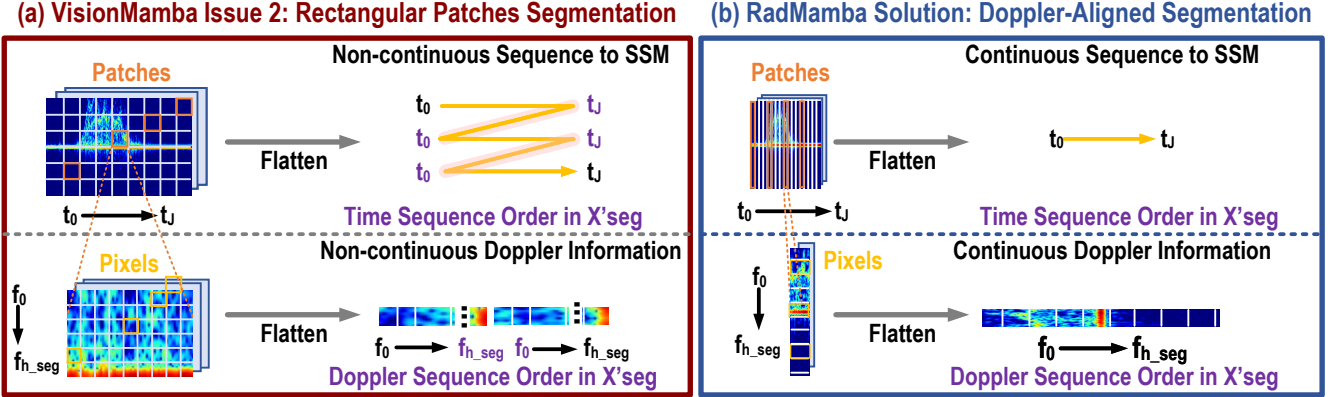


Fig. 2. VisionMamba Issue 2 and RadMamba Solution 2: Doppler-Aligned Segmentation

block is as follows:

$$\text{Chan-DS} = [(\text{Conv2D}, \text{BatchNorm}) \times L, \text{Maxpool2D}, \text{Maxpool1D}, \text{Avgpool1D (optional)}]$$

where  $L = 1, 2$ . The Two-Dimensional (2D) convolutional layer and batch normalization layer mix channel information and extract preliminary features from the input tensor  $\mathbf{X}$ . A 2D max pooling layer and a One-Dimensional (1D) max pooling layer reduce spatial dimensions. Optionally, an additional 1D average pooling layer further downsamples the time dimension if the data sparsity along the time axis is excessive for FMCW radar datasets.

This approach avoids generating numerous empty or redundant patches. Additionally, downsampling reduces the spatial dimensions before segmentation, thereby further contributing to an energy-efficient design.

### B. Solution 2: Doppler-Aligned Segmentation and Patch Embedding

The feature map after segmentation  $\mathbf{X}_{\text{seg}}$  has dimensions of  $C \times I \times J \times H_{\text{seg}} \times W_{\text{seg}}$ , where  $H_{\text{seg}}$  and  $W_{\text{seg}}$  denote the height and width of each patch. Thus, the number of patches per column and per row are determined by  $I = \frac{H}{H_{\text{seg}}}$  and  $J = \frac{W}{W_{\text{seg}}}$ , respectively, resulting in a total number of patches  $N = IJ$ .

As illustrated in Fig. 2 (a) (upper), patches indexed by  $j$  along the horizontal direction correspond to temporal positions  $t_j$ , where  $j = 0, 1, \dots, J$ . Within each patch, as shown in Fig. 2 (a) (bottom), pixels indexed by  $h_{\text{seg}}$  along the vertical direction correspond to Doppler frequency points  $f_{h_{\text{seg}}}$ , where  $h_{\text{seg}} = 0, 1, \dots, H_{\text{seg}}$ . Each patch is then flattened into a vector:

$$\mathbf{X}'_{\text{seg}} = \text{Flatten}(\mathbf{X}_{\text{seg}}) \quad (2)$$

where  $\mathbf{X}'_{\text{seg}} \in \mathbb{R}^{N \times CH_{\text{seg}}W_{\text{seg}}}$ .

The second limitation of conventional VisionMamba lies in the fact that patch flattening disrupts Doppler–temporal continuity, as depicted in Fig. 2 (a). On the one hand, rectangular segmentation results in a temporal ordering in  $\mathbf{X}'_{\text{seg}}$  along the dimension  $N$  of the form:

$$[t_0, t_1, \dots, t_J, t_0, t_1, \dots, t_J, \dots] \quad (3)$$

represented by the yellow folded arrow in Fig. 2 (a). Since VisionMamba treats  $N$  as a temporal evolution dimension in the SSM branches, the artificial jump from  $t_J$  to  $t_0$  introduces a temporal discontinuity, making it difficult for the SSM to extract meaningful temporal dynamics. On the other hand, the flattening operation yields a Doppler frequency sequence inside each patch of the form:

$$[f_0, f_1, \dots, f_{h_{\text{seg}}}, f_0, f_1, \dots, f_{h_{\text{seg}}}, \dots] \quad (4)$$

as shown in Fig. 2 bottom. The discontinuity between  $f_{h_{\text{seg}}}$  and  $f_0$  breaks the frequency pattern within each patch, simultaneously degrading both Doppler frequency consistency and the temporal evolution represented in that patch.

To address this issue, we propose Doppler-aligned segmentation, as shown in Fig. 2 (b):

$$\mathbf{X}_{\text{seg}} = \text{DA-Seg}(\mathbf{X}_{c-d}) \quad (5)$$

Specifically, we define patches with a height of  $H_{\text{seg}} = H_{c-d}$  (the full Doppler dimension) and a width of  $W_{\text{seg}} = 1$  (a single time bin of the spectrogram).

This Doppler-aligned segmentation ensures that the temporal evolution of the patch sequence remains strictly ordered as:

$$[t_0, t_1, \dots, t_J] \quad (6)$$

corresponding directly to the time sequence  $W$ . When the segmented data is fed into the SSM, as shown in Fig. 2 (b) (upper), the SSM receives a continuous temporal input stream. Furthermore, Doppler-aligned segmentation produces a patch vector with dimension

$$CH_{\text{seg}}W_{\text{seg}} = H_{c-d} \quad (7)$$

TABLE I  
AVERAGED CROSS-CORRELATION BETWEEN PATCHES BEFORE AND AFTER EACH PROJECTION LAYER.

	Linear Projection Layers in Conventional Mamba		Convolutional Projection Layers in Our Proposed CP-Mamba	
Projection	At Input	At Output	At Input	At Output
1	0.008	77.9	0.002	1065.7
2	0.008	0.4	0.002	16.1
3	160.1	75.5	245.3	356.4

preserving the entire Doppler profile within each patch. Consequently, after flattening, the Doppler frequency sequence remains intact as:

$$[f_0, f_1, \dots, f_{h\_seg}] \quad (8)$$

as illustrated in Fig. 2(b) (bottom). This maintains Doppler continuity, enabling the model to leverage fine-grained frequency dynamics without disruption.

### C. Solution 3: Convolution Projections in CP-Mamba Blocks

Within the conventional Mamba block (Fig. 1), the input  $\mathbf{X}_p$  is first normalized to obtain  $\mathbf{X}_{proj}$ , which is then split into three paths:

$$\mathbf{Z} = \text{Projection}_{P1}(\mathbf{X}_{proj}), \quad (9)$$

$$\mathbf{X}_{fw} = \text{Projection}_{P2}(\mathbf{X}_{proj}), \quad (10)$$

$$\mathbf{X}_{bw} = \text{Flip}(\mathbf{X}_{fw}, \text{dim} = \text{temporal dim.}), \quad (11)$$

where  $\mathbf{Z}, \mathbf{X}_{fw}, \mathbf{X}_{bw} \in \mathbb{R}^{N \times \text{dim}}$ , and  $\text{Flip}()$  reverses the temporal dimension of  $\mathbf{X}_{fw}$ .

In the conventional Mamba block,  $\text{Projection}_{P1}$  and  $\text{Projection}_{P2}$  are linear layers. In contrast, the CP-Mamba block replaces them with 1D convolutions using kernel size  $(\text{dim}, \text{dim}, 3)$ . Next,  $\mathbf{X}_{fw}$  and  $\mathbf{X}_{bw}$  are processed by the two SSM branches:

$$[\text{Conv1D}fw/bw, \text{LayerNorm}fw/bw, \text{SSM}fw/bw], \quad (12)$$

where  $\text{Conv1D}fw/bw$  has weight shape  $(\text{dim}, \text{dim}, 1)$  and operates along the sequence dimension  $(N, \text{dim})$ .

The two directional outputs are gated by the Sigmoid Linear Unit (SiLU)-activated  $\mathbf{Z}$  and summed:

$$\mathbf{Y}'fw/bw = \mathbf{Y}fw/bw \odot \text{SiLU}(\mathbf{Z}), \quad (13)$$

$$\mathbf{Y}sum = \mathbf{Y}'fw + \mathbf{Y}'bw, \quad (14)$$

where  $\odot$  denotes element-wise multiplication. Finally, a projection  $P3$  and residual connection produce the output:

$$\mathbf{Y}_{out} = \text{Projection}_{P3}(\mathbf{Y}_{sum}) + \mathbf{X}_{proj}, \quad (15)$$

In the conventional Mamba block, the projection layer  $P3$  is linear. In our CP-Mamba,  $P3$  is replaced with a Conv1D, where  $\text{Conv1D}_{P3}$  has weights  $(\text{dim}, \text{dim}, 1)$  and restores the sequence shape to  $(N, \text{dim})$ .

Ideally, projection layers should improve cross-correlation between patches, since a strong classifier should treat Doppler-aligned patches of the same activity as a coherent unit. Linear projections, however, increase correlation only marginally

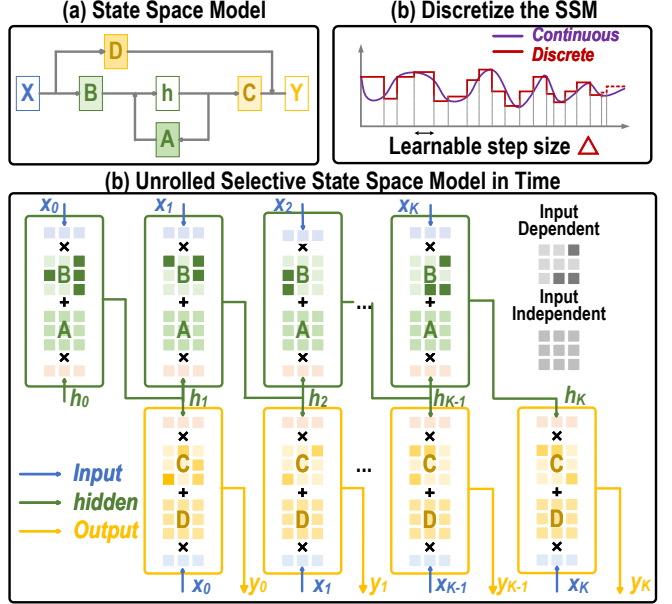


Fig. 3. The architecture of the State Space Model in RadMamba.

(P1, P2) or even reduce it (P3), limiting classification performance. The convolutional projections in CP-Mamba consistently strengthen cross-correlation, making patches easier to identify as belonging to the same action and improving Doppler-pattern sensitivity.

Tab. I reports the averaged patch cross-correlation using the Dataset CI4R [26]. For conventional linear projections, the averaged correlation before projections 1 and 2 is 0.008, rising to 0.77 and 0.4, respectively. Before and after projection 3, it drops from 160.1 to 75.5. In contrast, our convolutional projections greatly enlarge the correlation gap (e.g., from 77.9 to 1065.7 for P1), indicating superior ability to aggregate time bins of the same activity.

To compute the averaged patch cross-correlation, we train the model, freeze the parameters, and refeed the data. For  $\mathbf{X}_{proj} \in \mathbb{R}^{B \times N \times D}$ , each patch is indexed by  $n$ . The averaged cross-correlation is defined as:

$$\text{Corr}_{avg} = \frac{1}{B} \left( \frac{1}{N} \sum_{n=1}^N \left( \frac{1}{N} \sum_{n'=1}^N \text{corr}(\mathbf{X}_{proj}(\mathbf{b}, \mathbf{n}), \mathbf{X}_{proj}(\mathbf{b}, \mathbf{n}')) \right) \right) \quad (16)$$

where the correlation between two vectors of equal length is computed as:

$$\text{corr}(\mathbf{A}, \mathbf{B}) = \sum_{m=0}^M \sum_{m'=0}^M \mathbf{A}[m] \cdot \mathbf{B}[m + m'] \quad (17)$$

### D. Selective State-Space Modeling for Micro-Doppler Sequences

The SSM is a significant layer in CP-Mamba that enables efficient sequence modeling for the dynamic nature of micro-

Doppler signatures. As shown in Fig. 3 (a), the discrete SSM is defined as:

$$\mathbf{h}[n] = \bar{\mathbf{A}}[n]\mathbf{h}[n-1] + \bar{\mathbf{B}}[n]\mathbf{x}[n], \quad (18)$$

$$\mathbf{y}[n] = \mathbf{C}\mathbf{h}[n] + \mathbf{D}\mathbf{x}[n], \quad (19)$$

where the state transition  $\bar{\mathbf{A}}$  and the input matrices dimension  $\bar{\mathbf{B}}$  are discretized from corresponding matrices  $\mathbf{A}$  and  $\mathbf{B}$  in continuous SSM by a learnable step size  $\Delta$  as shown in Fig. 3 (b):

$$\bar{\mathbf{A}} = \exp(\Delta \cdot \mathbf{A}), \quad (20)$$

$$\bar{\mathbf{B}} = \left( \int_0^\Delta \exp(\mathbf{A}\tau) d\tau \right) \mathbf{B}, \quad (21)$$

The input of the SSM branches in the proposed CP-Mamba block are tensors  $\mathbf{X}_{fw/bw} \in \mathbb{R}^{N \times dim}$ ; after *Conv1D* and *LayerNorm* in SSM branch, this is termed as  $\mathbf{X}'_{fw/bw} \in \mathbb{R}^{N \times dim}$ .

Therefore, the discretized state-transition tensor  $\bar{\mathbf{A}}$  has dimension  $N \times dim \times dim_s$ , and the input tensor  $\bar{\mathbf{B}}$  has dimension  $N \times N \times dim_s$ . Here,  $N$  equals the time dimension in the micro-Doppler signatures. The input tensor  $\bar{\mathbf{B}}$  captures how the Doppler-aligned input vector influences the state  $\mathbf{h}[n]$ , whereas the state-transition tensor  $\bar{\mathbf{A}}$  captures how the previous state  $\mathbf{h}[n-1]$  contributes to  $\mathbf{h}[n]$ . Moreover, the matrices  $\mathbf{C} \in \mathbb{R}^{N \times dim_s}$  translate the current state  $\mathbf{h}[n]$  to the output. The skip matrices  $\mathbf{D} \in \mathbb{R}^{dim}$  add weighted input directly to the output of SSM, which helps the recurrent part focus on the temporal evolution.

The selective mechanism in the SSM introduces input-dependent parameterization that enhances adaptability as shown in Fig. 3 (c). The parameters  $\mathbf{B}$ ,  $\mathbf{C}$ , and  $\Delta$  are dynamically generated from the input sequence via linear projections:

$$\mathbf{B} = \mathbf{W}_B \mathbf{X}, \quad (22)$$

$$\mathbf{C} = \mathbf{W}_C \mathbf{X}, \quad (23)$$

$$\Delta = \text{Softplus}(\mathbf{W}_\Delta \mathbf{X}), \quad (24)$$

where  $\mathbf{W}_B$  and  $\mathbf{W}_C$  are weights of dimension  $(dim, dim_s)$ . The  $\Delta$  computation involves a linear layer with weights  $(dim, dt\_rank)$  followed by a projection to  $(N, dim)$  via weights  $(dt\_rank, dim)$ , where  $dt\_rank$  is a hyperparameter controlling the rank of the dynamic tensor. The Softplus activation ensures positive step sizes, implemented as  $\text{Softplus}(x) = \log(1 + \exp(x))$ .

### E. Overall Architecture

To summarize the method, the proposed RadMamba pipeline in pseudo-code is presented in Algorithm I. The patch embedding in *PEmb* follows the method in [18], and the position embedding method is a sinusoidal position encoding. [34].

## IV. OPEN-SOURCE DATASETS AND PREPROCESSING FOR RADAR-BASED HAR

To evaluate the efficacy of our proposed RadMamba framework, we utilize three distinct radar datasets. This section describes these datasets, namely the CW non-continuous Dataset

---

### Algorithm 1 Proposed RadMamba Pipeline

---

**Input:** Micro-Doppler Signature  $\mathbf{X} \in \mathbb{R}^{C \times H \times W}$

**Parameters:**  $dim, dim_s, dt\_rank$

**Output:** Classification Result  $\mathbf{F} \in \mathbb{R}^Q$ , where  $Q$  is the number of classes

- 1: **Channel Fusion and Downsample:**
- 2:  $\mathbf{X}_{c-d} = \text{Chan-DS}(\mathbf{X})$ ,  $\mathbf{X}_{c-d} \in \mathbb{R}^{C_{c-d} \times H_{c-d} \times W_{c-d}}$
- 3: **Doppler-Aligned Segmentation:**
- 4:  $\mathbf{X}_{seg} = \text{DA-Seg}(\mathbf{X}_{c-d})$ ,  $\mathbf{X}_{seg} \in \mathbb{R}^{C_{c-d} \times N \times H_{c-d}}$
- 5: **Patch and Position Embedding:**
- 6:  $\mathbf{X}'_p = \text{PEmb}(\mathbf{X}_{seg})$ ,  $\mathbf{X}'_p \in \mathbb{R}^{N \times D}$
- 7: **CP-Mamba Block:**
- 8:  $\mathbf{Y}_{out} = \text{CP-Mamba}(\mathbf{X}_p)$ ,  $\mathbf{Y}_{out} \in \mathbb{R}^{N \times dim}$
- 9: **Classify:**
- 10:  $\mathbf{F} = \mathbf{W}_{out} \mathbf{Y}_{out}$ ,  $\mathbf{F} \in \mathbb{R}^Q$

---

TABLE II

OVERVIEW OF RADAR-BASED HUMAN ACTIVITY RECOGNITION DATASETS USED IN THIS WORK.

Datasets	DIAT [25]	CI4R [26]	UoG20 [27]
Continuous Classes	No 6	No 11	Yes 6
Sensor Freq.(GHz)	X-band 10	IWR1443 77	FMCW 5.8
Resolution	224×224	224×224	240×1471
BW(MHz)	N/A	750	400
Length per sample (s)	3	20	35
Train Samples	2646	528	39
Test Samples	759	132	6
Sliding Window	N/A	N/A	224

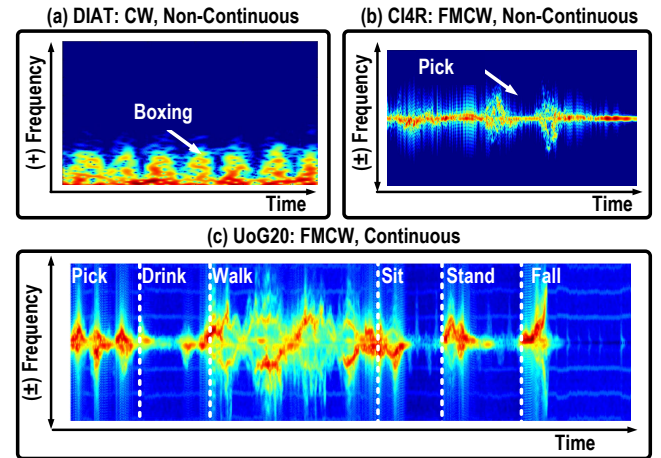


Fig. 4. Micro-Doppler Signature Example of (a) Dataset DIAT (b) Dataset CI4R (c) Dataset UoG20

DIAT, FMCW non-continuous Dataset CI4R, and FMCW continuous Dataset UoG20, along with their respective pre-processing steps. More details on these datasets are summarized in Tab. II. Here, the word ‘continuous’ refers to samples of data where sequences of human activities are continuously performed one after the other. Examples of micro-doppler signature after pre-processing are shown in Fig. 4.

### A. Dataset DIAT: X-Band CW Radar with Discrete Activity Instances [25]

This dataset was collected using an X-band CW radar operating at a frequency of 10 GHz. It encompasses data from 30 human subjects performing ‘suspicious’ activities at ranges spanning 10 meters to  $\pm 0.5$  kilometers over 3-second durations, resulting in an imbalanced set of 3,780 spectrogram samples of shape (3, 224, 224) across six activity classes. Preprocessing adheres to the methodology outlined in [25]. To facilitate a fair comparison with previous works, the dataset is partitioned into 70% training, 10% validation, and 20% test sets within each class, maintaining class-specific balance for reliable performance evaluation.

### B. Dataset CI4R: Short-Range FMCW Radar for Multi-Class Activity Recognition [26]

For the second dataset, experiments employ a Texas Instruments IWR1443 FMCW radar, operating at 77 GHz with a bandwidth of 750 MHz. It includes data from six participants, varying in age, height, and weight, performing 11 distinct activities and ambulatory gaits. Each participant executed 10 repetitions per activity, yielding 60 samples per class per sensor, as detailed in [26]. Preprocessing involves applying a 256-point short-time Fourier transform (Short-Time Fourier Transform (STFT)) with a context window length of 256 to convert the raw radar signals into a 2D micro-Doppler representation of shape (1, 224, 224). The dataset is split with an 8:2 training-to-test ratio, ensuring sufficient data for model optimization and evaluation.

### C. Dataset UoG2020: Continuous FMCW Radar for Realistic HAR Sequences [27]

Representing a leap in complexity, this dataset was acquired using an FMCW radar operating at 5.8 GHz with a 400 MHz bandwidth. It comprises data from 15 participants (14 males, 1 female, aged 21–35) performing six basic activities within continuous 35-second sequences. These activities are organized into three distinct sequential orders, with participants granted autonomy in selecting transition points between consecutive activities and determining trajectories for translational tasks, as described in [27]. The resulting micro-Doppler signatures are preprocessed into (1, 240, 224) 2D frames, with data from two participants designated as the test set and data from the remaining 13 participants used for training, providing a challenging benchmark for continuous sequence modeling.

## V. EXPERIMENTAL SETUP

### A. Network Structure

The classification performance of RadMamba is evaluated against a suite of established models, selected for their proven efficacy across CNN, RNN, and hybrid architectures: customized ResNet6 [35], Bi-LSTM [27], CNN-LSTM [16], and CNN-Bi-GRU [17]. To explore the impact of model scaling, we conducted a model size sweep experiment, varying the hidden dimensions as shown in Tab. III. These sizes are chosen to capture the full spectrum of performance trends as

TABLE III  
NETWORK ARCHITECTURE OF MODELS USED IN THIS WORK

Model	Swept Hidden Size ( <i>dim</i> for RadMamba)
ResNet6 (Customized)	5, 7, 12, 20, 30
Bi-LSTM	1, 2, 4, 10, 20, 28, 34
CNN-LSTM	2, 4, 6, 16, 28, 34, 46
CNN-Bi-GRU	1, 2, 4, 6, 16, 28
RadMamba Dataset DIAT	8, 16, 32, 64, 80
RadMamba Dataset CI4R	8, 16, 32, 64, 80, 96, 128, 160
RadMamba Dataset UoG20	8, 16, 20, 24, 32

TABLE IV  
SPECIFIED NETWORK ARCHITECTURE VARIATIONS OF RADMAMBA

Datasets	<i>dim<sub>s</sub></i>	<i>dt_rank</i>	Chan. Fusion	DS Redu. Factor
Dataset DIAT	1	2	2, (16, 3, 3)	(2, 2)
Dataset CI4R	4	0	1, (1, 3, 3)	(2, 8)
Dataset UoG20	16	4	1, (1, 3, 3)	(2, 32)

model capacity increases, providing insights into scalability and efficiency.

The customized ResNet6 is derived from ResNet18 by preserving the first five layers and the final classifier while maintaining its channel ratio between consecutive channels. The minimum channel width is tunable to target low-FLOP regimes, enabling fair comparisons under limited computation conditions. Although the CNN-Bi-GRU retains a larger parameter budget, its fusion strategy may not generalize consistently across datasets.

All four baselines (ResNet6, Bi-LSTM, CNN-LSTM, and CNN-Bi-GRU) are retrained from scratch in a unified PyTorch pipeline, using consistent dataset splits, preprocessing, optimization settings, and batch=1 memory profiling. For transformer and SSM competitors, FML-ViT [19], LW-ViT [33], and ActivityMamba [22], we report their best published small-scale configurations. Following their protocols, we adopt the same training settings for FML-ViT and ActivityMamba, but use a different input size than LW-ViT: their preprocessing produces 656×656 inputs on the CI4R dataset, whereas our pipeline uses 224×224.

For RadMamba, the configurations of channel fusion, down-sampling, and SSM parameters are dataset-specific to optimize micro-Doppler processing (Tab. IV). The ‘channel fusion’ column specifies [L, (C<sub>c-d</sub>, H<sub>k</sub>, W<sub>k</sub>)], where L is the number of channel fusion blocks and the C<sub>c-d</sub>, H<sub>k</sub>, W<sub>k</sub> are channel, kernel height, kernel width of Conv2D layer, respectively. The ‘DS Redu. Factor’ denotes the reduction factors (H/H<sub>c-d</sub>, W/W<sub>c-d</sub>).

Hyperparameter selection follows two principles:

- **Bayesian optimization:** Because RadMamba is highly configurable, we perform a Bayesian-optimization-based search over a constrained space. Since *dim* predominantly determines the sizes of most weight matrices, the number of channels in *Chan-DS*, *dim<sub>s</sub>*, and *dt<sub>rank</sub>* were selected to minimize model complexity across different *dim*.
- **Physical perspective from micro-Doppler signature (Temporal downsampling and Reduction Factor):** The first downsampling factor of 2 × 2 in *Chan-DS* matches

the fact that most Doppler energy appears in the central part of the spectrum. With horizontal reduction factors of 8 and 32 for the *CI4R* and *UoG20* datasets (as shown in Tab. IV), each Doppler vector spans approximately 640 ms. Empirically, this temporal interval provides an optimal balance for both FMCW datasets.

### B. Training Hyperparameter

Training is conducted using the Adaptive Moment Estimation with decoupled Weight decay (AdamW) optimizer [36], [37], paired with the ReduceLROnPlateau scheduler, which adjusts the learning rate adaptively based on test performance. For Dataset DIAT, the initial learning rate is set to  $1 \times 10^{-4}$ , with a batch size of 16, and training proceeds for 50 epochs. For Dataset CI4R, RadMamba employs an initial learning rate of  $5 \times 10^{-3}$ , while the baseline models use  $1 \times 10^{-4}$ , with a batch size of 16 over 100 epochs, reflecting the dataset's increased complexity and sample size. For Dataset UoG20, the initial learning rate is  $5 \times 10^{-5}$ , with a larger batch size of 256 and 50 epochs, processing continuous sequences with a frame length of 224 and a stride of 1 to effectively capture temporal dependencies. All experiments are executed on a single NVIDIA RTX 4090 GPU.

To account for training variability, all models, including RadMamba, are trained and evaluated ten times with distinct seeds. The following analysis reports the mean and standard deviation of performance metrics from the model size swept experiment.

### C. Evaluation Settings

Inference time and memory profiling are conducted on an NVIDIA Jetson Orin Nano Developer Kit with PyTorch 2.8.0 and CUDA 12.6. The kit is equipped with a 6-core Arm Cortex-A78AE CPU and an NVIDIA Ampere Architecture GPU with unified off-chip 8 GB 128-bit LPDDR5 memory. The evaluation follows a standardized protocol: each model undergoes 10 warm-up iterations followed by 100 measurement iterations, with inference performed at a batch size of 1. Peak memory (Peak Mem.) is measured using `torch.cuda.memory_allocated(device)`, which returns the maximum allocated memory across all 100 inference iterations. CUDA synchronization with the ARM CPU is enforced before and after each forward pass to ensure accurate timing measurements.

## VI. RESULTS AND DISCUSSION

### A. Comparison with Previous Works

The experimental results detailed in Table V highlight the superior performance of our proposed RadMamba model across multiple radar-based human activity recognition datasets.

Figure 5 (a) and (b) present confusion matrices comparing the ground truth labels with the best predictions of RadMamba, illustrating its classification accuracy and error distribution for each dataset. Figure 5 (c) shows the comparison between

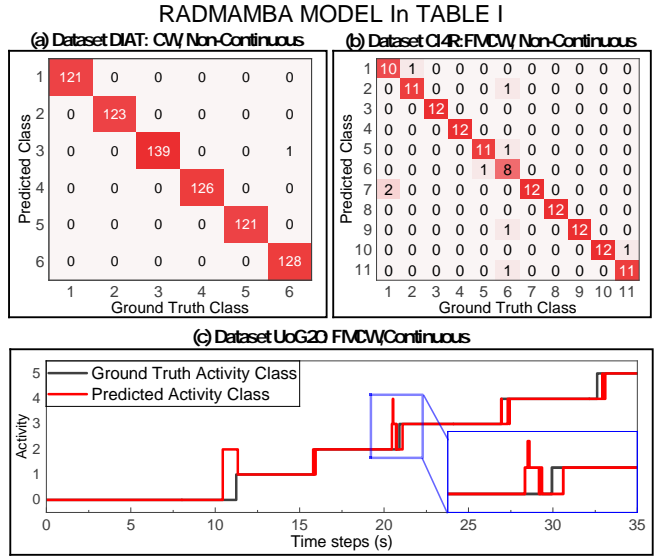


Fig. 5. Example of comparisons between ground truth and best prediction of RadMamba model with the configuration in Table I on (a) Dataset DIAT; (b) Dataset CI4R; (c) Dataset UoG20.

the classification results of RadMamba and CNN-LSTM over time.

On Dataset DIAT, which utilizes CW radar in a non-continuous setting, RadMamba achieved an accuracy of 99.8% with a standard deviation of  $\pm 0.12\%$ , using only 21.7k parameters and requiring 145.6 million #FLOP/Inf. per sample. This demonstrates its capability to match the state-of-the-art accuracy of previous models while being significantly more parameter-efficient compared to  $\sim 8700$ k parameters and computationally lighter compared to  $\sim 1220$ M #FLOP per inference. The CNN-LSTM with 8.7 M #FLOP per inference achieves better accuracy of 98.4% than 98.2% from RadMamba with 14.5 M #FLOP per inference. Taking 45 nm technology as an example, the energy consumption of an 8 kB SRAM access for one 32-bit floating-point parameter and one 32-bit floating-point operation is 5.0 pJ and 4.6 pJ, respectively [38]. With an 11 $\times$  larger model and only about half the #FLOPs per inference, it is unlikely that the CNN-LSTM can be more energy-efficient than RadMamba.

For Dataset CI4R, employing FMCW radar in a non-continuous scenario with 11 activities, RadMamba attained an accuracy of 91.2% with a standard deviation of  $\pm 2.57\%$ , leveraging 71.4 thousand parameters. This performance outperforms previous models shown in Tab. V. Moreover, it remains competitive with the state-of-the-art of previous models while requiring substantially fewer computational resources (8.8 M #FLOP/Inf. vs. 169 M to 2410 M #FLOP/Inf., showcasing its ability to excel in more complex activity recognition tasks with minimal computational overhead. Moreover, compared to the Bi-LSTM model, which has the lowest arithmetic intensity among the baselines, RadMamba improves accuracy by 9.4 percentage points while using 86.5 k fewer parameters and the same 6.0 M #FLOP/Inf.

On Dataset UoG20, which involves FMCW radar in a continuous setting with 6 activities, RadMamba recorded an

TABLE V

MEAN AND STANDARD DEVIATION OF CLASSIFICATION ACCURACY PERFORMANCE ACROSS SEED 0 TO 9 OF DIFFERENT NN-BASED RADHAR MODELS EVALUATED WITH THREE DIFFERENT RADAR SETTINGS ALONGSIDE THEIR MODEL SIZE AND FLOATING-POINT OPERATIONS (#FLOP.)

Classifiers	Dataset DIAT [25] (CW, Non-continuous)					Dataset CI4R [26] (FMCW, Non-continuous)					Dataset UoG20 [27] (FMCW, Continuous)				
	#params (k)	#FLOP <sup>a</sup> (M)	Accuracy (%)	Peak Mem (MB)	Inf. Time (ms)	#params (k)	#FLOP <sup>a</sup> (M)	Accuracy (%)	Peak Mem. (MB)	Inf. Time (ms)	#params (k)	#FLOP <sup>a</sup> (M)	Accuracy (%)	Peak Mem. (MB)	Inf. Time (ms)
ResNet6 <sup>b</sup> [35]	69.4	253.3	99.8 $\pm$ 0.16	11.9	4.8	150.7	310.2	32.3 $\pm$ 3.35	12.8	5.1	24.7	72.8	83.6 $\pm$ 1.73	10.7	4.8
Bi-LSTM [27]	23.3	5.6	93.9 $\pm$ 0.68	10.5	1188.4	134.4	6.0	79.4 $\pm$ 1.23	10.2	1173.4	15.5	2.1	85.3 $\pm$ 2.01	9.7	1162.9
CNN-LSTM [16]	115.3	8.7	98.4 $\pm$ 0.33	11.1	214.6	96.5	8.7	86.1 $\pm$ 1.32	10.0	212.0	10.3	1.2	86.1 $\pm$ 2.22	11.0	209.7
CNN-Bi-GRU [17]	55.0	1090.1	98.5 $\pm$ 0.41	22.3	1314.5	142.8	1013.0	84.9 $\pm$ 1.11	22.2	1305.5	53.6	1082.0	85.4 $\pm$ 2.19	22.8	1291.9
FML-VIT <sup>c</sup> [19]	-	-	-	-	-	$\sim$ 2700	169.0	$\sim$ 92.0	-	-	-	-	-	-	-
LW-VIT <sup>c</sup> [33]	-	-	-	-	-	769	$\sim$ 2410	$\sim$ 92.0	-	-	-	-	-	-	-
ActivityMamba <sup>c</sup> [22]	$\sim$ 8700.0	$\sim$ 1220.0	99.8	-	-	-	-	-	-	-	-	-	-	-	-
<b>RadMamba (Ours)</b>	<b>21.7</b>	<b>145.6</b>	<b>98.8<math>\pm</math>0.12</b>	<b>16.5</b>	<b>21.2</b>	<b>71.4</b>	<b>8.8</b>	<b>91.2<math>\pm</math>2.57</b>	<b>10.2</b>	<b>15.1</b>	<b>6.7</b>	<b>1.0</b>	<b>89.3<math>\pm</math>1.38</b>	<b>10.0</b>	<b>11.6</b>
<b>RadMamba (Ours)</b>	<b>10.1</b>	<b>14.5</b>	<b>98.2<math>\pm</math>0.46</b>	<b>16.5</b>	<b>21.2</b>	<b>47.9</b>	<b>6.0</b>	<b>88.8<math>\pm</math>4.58</b>	<b>10.1</b>	<b>14.9</b>	<b>17.7</b>	<b>1.8</b>	<b>89.6<math>\pm</math>0.78</b>	<b>10.0</b>	<b>12.6</b>

<sup>a</sup> #FLOP. is the number of floating-point operations per inference.

<sup>b</sup> This ResNet6 only retains the first 5 layers and the output linear layers of ResNet18.

<sup>c</sup> The ‘ $\sim$ ’ indicates that these results are approximated from the references [19], [22], [33].

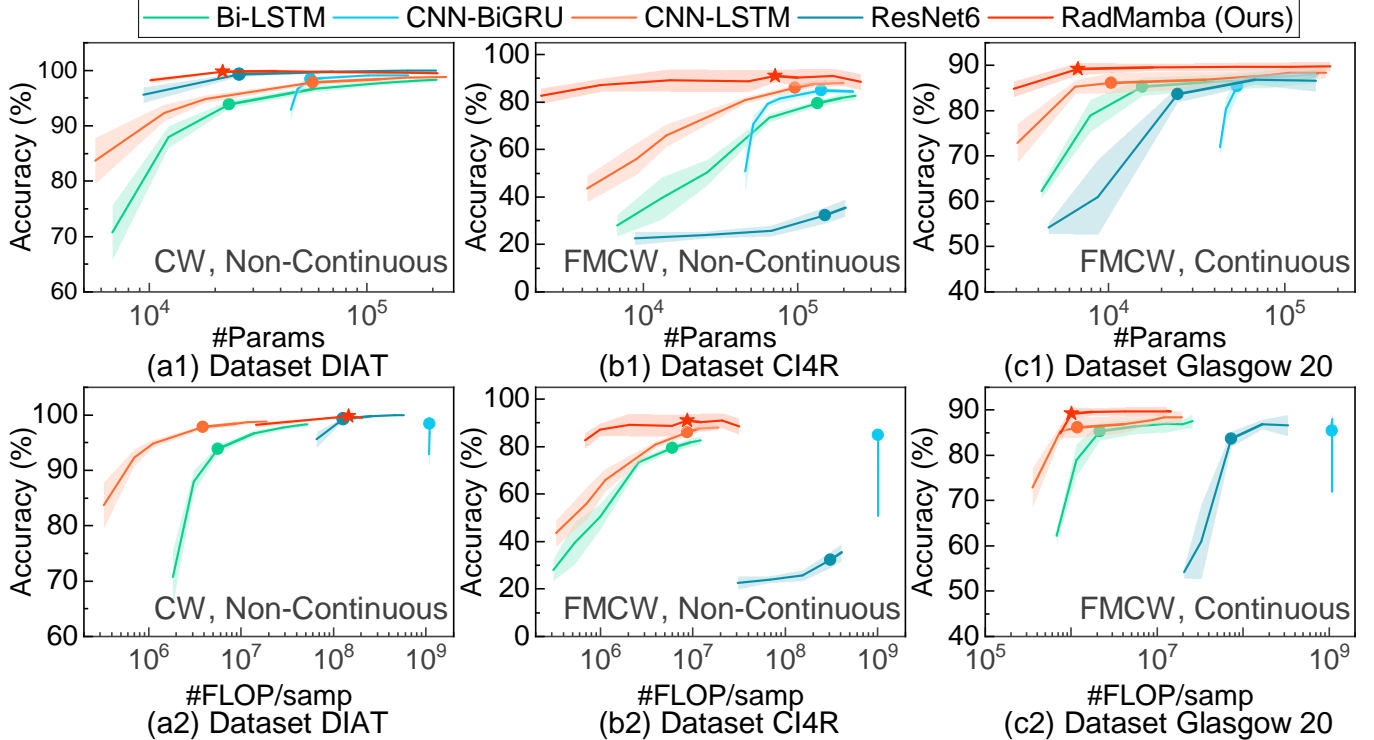


Fig. 6. Accuracy vs. number of parameters (1) and number of #FLOP/Inf. (2) on: (a) Dataset DIAT (b) Dataset CI4R (c) Dataset UoG20

accuracy of 89.3% with a standard deviation of  $\pm 1.38\%$ , utilizing 6.7 thousand parameters and 1.0M #FLOP/Inf. per inference. With an even smaller model size and a more complicated task than in Datasets DIAT and CI4R, RadMamba achieves the best accuracy among the models shown in Tab. V and highlights its effectiveness in continuous HAR scenarios with the smallest model size and #FLOP/Inf. per inference.

Regarding inference time performance, as detailed in Tab. V, RadMamba demonstrates a substantial speedup compared to RNN-based and hybrid models, achieving 10 to 100 $\times$  faster inference. For instance, on Dataset CI4R, RadMamba (71.4k parameters) achieves an inference time of 15.13 ms. This represents a 78 $\times$  speedup over Bi-LSTM and an 87 $\times$  speedup over CNN-Bi-GRU. While the conventional CNN model, ResNet6, exhibits faster inference times (e.g., 5.14 ms on the CI4R dataset), its accuracy is significantly lower

(32.3% vs. RadMamba’s 91.2%). This result highlights RadMamba’s superior trade-off between accuracy and efficiency, which is critical for reliable real-time RadHAR applications.

We also measured peak memory consumption to address concerns about efficiency. The results in Tab. V reveal relatively small differences between models, with peak CUDA allocated memory ranging from 9.7 MB to 22.8 MB. This limited variation, despite RadMamba’s significantly smaller parameter count, highlights a limitation of benchmarking on general-purpose, throughput-oriented embedded GPU architectures for edge inference when the batch size equals 1. On such platforms, the memory footprint is dominated by system-level overheads, such as CUDA context initialization, driver memory pools, and memory management, which mask the model’s intrinsic parameter efficiency.

The true advantage of RadMamba’s parameter efficiency

is its suitability for future hardware-software co-design. Its minimal footprint, ranging from 6.7k to 71.4k parameters across the three tested datasets, is intended to enable the entire model to be buffered within on-chip SRAM on a dedicated RadHAR accelerator. This approach would eliminate power-hungry off-chip DDR memory accesses, a primary source of power consumption in on-sensor systems. This fundamental power-saving benefit, along with the low arithmetic utilization for batch-size-1 inference on GPUs, cannot be captured by measurements on the Jetson platform. Therefore, we contend that the #params and #FLOPs metrics reported in Tab. V are more representative indicators of the RadMamba’s potential for enabling ultra-low-power, on-sensor inference, which is the primary goal of this work.

### B. Model Scaling and Efficiency Analysis

The model size swept results, illustrated in Figure 6, compare accuracy against the number of parameters from 2k to 150k and #FLOP/Inf. across Datasets DIAT, CI4R, and UoG20 between previous models ResNet6, Bi-LSTM, CNN-Bi-GRU, and CNN-LSTM and the proposed RadMamba.

For Dataset DIAT, as presented in Fig. 6 (a1) and (a2), RadMamba achieves a peak accuracy of 99.8% with only 21.7k parameters. However, RadMamba overfits with a model size larger than 21.7k because the dataset is very simple and the accuracy is close to 100%. In contrast, ResNet6’s accuracy increases steadily with model size, reaching 99.9% with 208.1k parameters, yet it requires nearly ten times the parameters of RadMamba for slightly lower performance.

On Dataset CI4R, as shown in Fig. 6 (b1) and (b2), RadMamba consistently outperforms previous models across a range of parameter configurations in efficiency, maintaining superior accuracy with fewer parameters and #FLOP/Inf. Similarly, for Dataset UoG20 shown in Fig. 6 (c1) and (c2), RadMamba still records a higher accuracy for continuous activities scenarios with fewer #FLOP/Inf., outperforming larger and more computationally intensive models in efficiency and effectiveness.

These trends, as depicted in the figure, affirm RadMamba’s capability to achieve superior accuracy across diverse radar modalities while drastically reducing both parameter count and #FLOP/Inf., positioning it as an optimal solution for lightweight, real-time human activity recognition.

### C. Ablation study of the Micro-doppler-oriented Structure

Table VI presents an ablation study evaluating the impact of new architectural blocks in the RadMamba model across three datasets with varying radar settings. The study systematically assesses the effects of different projection layers, patch sizes, and downsampling scales on model accuracy and parameter efficiency, with results averaged over seeds 0 to 5.

The main conclusion from this ablation study is that optimal performance emerges from the combined use of all three proposed new blocks, including the projection layer, the patch size, and the downsampling scale, rather than any single component in isolation. This is evident in the incremental improvements observed across the configurations. For instance,

the baseline conventional ViM model (Row 1) achieves an accuracy of 93.5% on Dataset DIAT, 61.9% on Dataset CI4R, and 71.2% on Dataset UoG20. In contrast, the proposed RadMamba (Row 27), which incorporates a 1D convolution layer, a patch size of  $(H_{c-d}, 1)$ , and a downsampling (2, 2), achieves a higher accuracy of 99.8% on Dataset DIAT. Similarly, on Dataset CI4R, Row 27 with a (2, 8) downsampling scale yields significantly higher accuracy of 89.6%, and on Dataset UoG20 with a (2, 32) scale, it reaches 88.6%. Intermediate configurations, such as Row 19 (only projection replacement), Row 7 (only patch size changing), and Row 2 (only downsampling applied) show lower accuracies—underscoring that no single structure alone achieves the peak performance of the fully combined design in Row 27.

To provide a more detailed analysis, we discuss the three blocks—projection layer, patch size, and downsampling scale—separately, evaluating their individual contributions to RadMamba’s performance across the datasets.

1) *Projection Replacement*: The adoption of a 1D convolutional layer as the projection mechanism consistently outperforms configurations with a single linear layer or three linear layers across nearly all settings. Comparing Rows 19-27 with Rows 10-18 and Rows 1-9, the conv1d projection replacement within the same patch size and downsampling scale achieved an average increment of mean accuracy by 0.48% over 1 linear layer, 0.40% over 3 linear layers on Dataset DIAT. On datasets CI4R and UoG20, the conv1d layer shows a substantial improvement of 2.99% and 3.64% over 1 linear layer, respectively.

2) *Patch Size*: The  $(H_{c-d}, 1)$  configuration consistently delivers superior performance within each projection layer type. For the 1D convolutional layer, Row 25 with  $(H_{c-d}, 1)$  and without downsampling achieves 3% gain on Dataset DIAT, 22.4% gain on Dataset CI4R, 9.2% gain on Dataset UoG20 vs. Row 19 with rectangular patch. This trend holds across other projection types, indicating that the  $(H_{c-d}, 1)$  patch size effectively retains the critical spatial features for radar data processing.

3) *Downsampling*: The results suggest that downsampling along the patch vector dimension generally outperforms downsampling along the dimension orthogonal to the patch vector and no downsampling. For instance, Row 27’s (2, 32) time downsampling achieves  $88.6\% \pm 1.46$ , outperforming Row 26’s (8, 2) at  $84.4\% \pm 2.05$  and Row 25’s (1, 1) at  $84.5\% \pm 0.77$  on Dataset UoG20. This pattern highlights the advantage of downsampling in enhancing the micro-Doppler features.

The ablation study underscores the efficacy of the proposed RadMamba design, with the highest performance achieved by integrating a 1D convolutional projection layer, a  $(H_{c-d}, 1)$  patch size, and time-dimension downsampling (Row 27).

## VII. CONCLUSION

RadMamba sets a new benchmark in RadHAR (Code: <https://github.com/lab-emi/AIRHAR>), delivering top-tier accuracy with minimal parameters and computational cost across diverse datasets. Its radar micro-Doppler-oriented design addresses domain-specific challenges, making it ideal for real-time, resource-constrained applications. Overall, RadMamba

TABLE VI

ABLATION STUDY WITH PROGRESSIVE TECHNIQUES (DENOTED BY **Tech.**) OF NEW BLOCKS IN RADMAMBA ACROSS SEED 0 TO 5, EVALUATED WITH THREE DIFFERENT RADAR SETTINGS ALONGSIDE THEIR NUMBER OF PARAMETERS

Row	Tech. 1: Proj. Layer	Tech. 2: Patch Size	Dataset DIAT			Dataset CI4R			Dataset UoG20		
			Tech. 3: Down-sample.	Accuracy (%)	#Params (k)	Tech. 3: Down-sample.	Accuracy (%)	#Params (k)	Tech. 3: Down-sample.	Accuracy (%)	#Param (k)
1 (Conventional)	1 linear layer	$(H_{seg}, W_{seg})^a$	(1, 1)	93.5 $\pm$ 1.06	11.3	(1, 1)	61.9 $\pm$ 2.55	40.6	(1, 1)	71.2 $\pm$ 2.10	4.2
2			-	-	-	$\hat{\wedge}$ (8, 2)	71.6 $\pm$ 2.42	40.6	$\hat{\wedge}$ (8, 2)	80.1 $\pm$ 2.07	4.2
3			(2, 2)	99.6 $\pm$ 0.06	11.3	$\hat{\wedge}$ (2, 8)	63.0 $\pm$ 7.75	40.6	$\hat{\wedge}$ (2, 32)	66.9 $\pm$ 2.01	4.2
4			(1, 1)	87.7 $\pm$ 1.25	39.3	(1, 1)	67.9 $\pm$ 0.76	54.9	(1, 1)	72.6 $\pm$ 2.20	7.6
5			-	-	-	$\hat{\wedge}$ (8, 2)	65.2 $\pm$ 2.73	45.8	$\hat{\wedge}$ (8, 2)	67.7 $\pm$ 1.27	5.5
6			(2, 2)	98.5 $\pm$ 0.43	21.4	$\hat{\wedge}$ (2, 8)	77.3 $\pm$ 2.80	38.9	$\hat{\wedge}$ (2, 32)	64.0 $\pm$ 1.26	3.6
7			(1, 1)	96.9 $\pm$ 0.52	39.3	(1, 1)	88.4 $\pm$ 0.76	54.9	(1, 1)	83.9 $\pm$ 1.85	7.8
8			$(H_{c-d}, 1)$	-	-	$\hat{\wedge}$ (8, 2)	84.6 $\pm$ 4.12	38.9	$\hat{\wedge}$ (8, 2)	84.3 $\pm$ 1.88	4.1
9			(2, 2)	99.9 $\pm$ 0.00	21.4	$\hat{\wedge}$ (2, 8)	86.5 $\pm$ 4.35	45.8	$\hat{\wedge}$ (2, 32)	84.2 $\pm$ 2.00	5.7
10	3 linear layer <sup>b</sup>	$(H_{seg}, W_{seg})^a$	(1, 1)	92.6 $\pm$ 0.98	11.6	(1, 1)	40.1 $\pm$ 11.98	66.2	(1, 1)	70.6 $\pm$ 2.12	5.2
11			-	-	-	$\hat{\wedge}$ (8, 2)	69.9 $\pm$ 2.99	66.2	$\hat{\wedge}$ (8, 2)	78.2 $\pm$ 3.66	5.2
12			(2, 2)	99.5 $\pm$ 0.10	11.6	$\hat{\wedge}$ (2, 8)	57.8 $\pm$ 9.64	66.2	$\hat{\wedge}$ (2, 32)	68.5 $\pm$ 1.50	5.2
13			(1, 1)	88.8 $\pm$ 2.42	39.6	(1, 1)	48.3 $\pm$ 9.80	80.5	(1, 1)	70.8 $\pm$ 2.43	8.6
14			-	-	-	$\hat{\wedge}$ (8, 2)	43.3 $\pm$ 8.54	71.4	$\hat{\wedge}$ (8, 2)	65.2 $\pm$ 1.48	6.6
15			(2, 2)	98.7 $\pm$ 0.32	21.7	$\hat{\wedge}$ (2, 8)	72.4 $\pm$ 3.12	64.5	$\hat{\wedge}$ (2, 32)	64.0 $\pm$ 2.16	4.7
16			(1, 1)	97.2 $\pm$ 0.26	39.6	(1, 1)	85.3 $\pm$ 1.27	80.5	(1, 1)	83.6 $\pm$ 1.04	8.9
17			$(H_{c-d}, 1)$	-	-	$\hat{\wedge}$ (8, 2)	83.9 $\pm$ 1.71	64.5	$\hat{\wedge}$ (8, 2)	83.2 $\pm$ 1.64	5.1
18			(2, 2)	99.8 $\pm$ 0.06	21.7	$\hat{\wedge}$ (2, 8)	85.3 $\pm$ 2.67	71.4	$\hat{\wedge}$ (2, 32)	85.2 $\pm$ 1.16	6.7
27 (Ours)	1 conv1d layer <sup>c</sup>	$(H_{seg}, W_{seg})^a$	(1, 1)	93.8 $\pm$ 1.14	11.6	(1, 1)	65.5 $\pm$ 3.30	66.2	(1, 1)	75.3 $\pm$ 2.34	5.2
20			-	-	-	$\hat{\wedge}$ (8, 2)	75.0 $\pm$ 2.45	66.2	$\hat{\wedge}$ (8, 2)	81.0 $\pm$ 2.10	5.2
21			(2, 2)	99.6 $\pm$ 0.15	11.6	$\hat{\wedge}$ (2, 8)	70.7 $\pm$ 3.23	66.2	$\hat{\wedge}$ (2, 32)	74.3 $\pm$ 2.31	5.2
22			(1, 1)	90.1 $\pm$ 1.72	39.6	(1, 1)	70.7 $\pm$ 3.43	80.5	(1, 1)	76.4 $\pm$ 2.77	8.6
23			-	-	-	$\hat{\wedge}$ (8, 2)	69.3 $\pm$ 3.09	71.4	$\hat{\wedge}$ (8, 2)	74.4 $\pm$ 3.26	6.6
24			(2, 2)	98.9 $\pm$ 0.13	21.7	$\hat{\wedge}$ (2, 8)	79.0 $\pm$ 2.42	64.5	$\hat{\wedge}$ (2, 32)	68.8 $\pm$ 2.08	4.7
25			(1, 1)	96.8 $\pm$ 0.86	39.6	(1, 1)	87.9 $\pm$ 0.36	80.5	(1, 1)	84.5 $\pm$ 0.77	8.9
26			$(H_{c-d}, 1)$	-	-	$\hat{\wedge}$ (8, 2)	85.6 $\pm$ 3.16	64.5	$\hat{\wedge}$ (8, 2)	84.4 $\pm$ 2.05	5.1
27 (Ours)			(2, 2)	99.8 $\pm$ 0.11	21.7	$\hat{\wedge}$ (2, 8)	89.6 $\pm$ 3.69	71.4	$\hat{\wedge}$ (2, 32)	88.6 $\pm$ 1.46	6.7

<sup>a</sup>  $(H_1, W_1)$  equals to (7, 7) for Dataset DIAT and B, (5, 7) for Dataset UoG20 due to the different image size of these datasets.

<sup>b</sup> This option replaces projections 1 and 2 from a single linear layer to three linear layers.

<sup>c</sup> The kernel size for projection 1 and 2 is  $(dim, dim, 3)$ , and for projection 3 is  $(dim, dim, 1)$ .

consistently outperforms previous neural network models like ResNet6, Bi-LSTM, CNN-LSTM, and CNN-Bi-GRU, and competes with or exceeds advanced architectures like Vision Transformers and ActivityMamba, all while maintaining a remarkably low parameter count (ranging from 6.7k to 71.4k) and reduced computational complexity (1.3M to 145.6M #FLOP/Inf.). These results emphasize RadMamba's capability as a lightweight and high-performance solution for radar-based HAR across diverse radar modalities and activity recognition tasks. The micro-Doppler-oriented design, which integrates channel fusion, Doppler-aligned segmentation, and convolutional projections, addresses the unique challenges of radar data, delivering to deliver high accuracy across both CW and FMCW datasets, both including continuous and non-continuous data. Ablation studies confirm the synergy of its components, with no single element achieving comparable performance on its own.

#### ACKNOWLEDGMENTS

This work is funded by the European Research Executive Agency (REA) under the Marie Skłodowska-Curie Actions (MSCA) Postdoctoral Fellowship program, Grant No. 101107534 (AIRHAR). We thank Prof. Dr. L.C.N. de Vreede and Prof. Dr. Alexander Yarovoy for their support.

#### REFERENCES

- X. Li, Y. He, and X. Jing, "A survey of deep learning-based human activity recognition in radar," *Remote Sensing*, vol. 11, no. 9, 2019. [Online]. Available: <https://www.mdpi.com/2072-4292/11/9/1068>
- I. Ullmann, R. G. Guendel, N. C. Kruse, F. Fioranelli, and A. Yarovoy, "A survey on radar-based continuous human activity recognition," *IEEE Journal of Microwaves*, vol. 3, no. 3, pp. 938–950, 2023.
- Y. Kim and H. Ling, "Human activity classification based on micro-doppler signatures using a support vector machine," *IEEE Transactions on Geoscience and Remote Sensing*, vol. 47, no. 5, pp. 1328–1337, 2009.
- M. Zenaldin and R. M. Narayanan, "Radar micro-Doppler based human activity classification for indoor and outdoor environments," in *Radar Sensor Technology XX*, K. I. Ranney and A. Doerry, Eds., vol. 9829, International Society for Optics and Photonics. SPIE, 2016, p. 98291B. [Online]. Available: <https://doi.org/10.1117/12.2228397>
- B. Erol, M. Francisco, A. Ravishankar, and M. Amin, "Realization of radar-based fall detection using spectrograms," in *Compressive Sensing VII: From Diverse Modalities to Big Data Analytics*, F. Ahmad, Ed., vol. 10658, International Society for Optics and Photonics. SPIE, 2018, p. 106580B. [Online]. Available: <https://doi.org/10.1117/12.2309817>
- H. Li, A. Shrestha, H. Heidari, J. L. Kerne, and F. Fioranelli, "Activities recognition and fall detection in continuous data streams using radar sensor," in *2019 IEEE MTT-S International Microwave Biomedical Conference (IMBioC)*, vol. 1, 2019, pp. 1–4.
- H. Li, A. Shrestha, H. Heidari, J. Le Kerne, and F. Fioranelli, "Bi-lstm network for multimodal continuous human activity recognition and fall detection," *IEEE Sensors Journal*, vol. 20, no. 3, pp. 1191–1201, 2020.
- R. G. Guendel, F. Fioranelli, and A. Yarovoy, "Distributed radar fusion and recurrent networks for classification of continuous human activities," *IET Radar, Sonar & Navigation*, vol. 16, no. 7, pp. 1144–1161, 2022. [Online]. Available: <https://ietresearch.onlinelibrary.wiley.com/doi/abs/10.1049/rsn2.12249>
- C. Ding, H. Hong, Y. Zou, H. Chu, X. Zhu, F. Fioranelli, J. Le Kerne, and C. Li, "Continuous human motion recognition with a dynamic range-doppler trajectory method based on fmcw radar," *IEEE Transactions on Geoscience and Remote Sensing*, vol. 57, no. 9, pp. 6821–6831, 2019.
- Y. Kim and T. Moon, "Human detection and activity classification based on micro-doppler signatures using deep convolutional neural networks," *IEEE Geoscience and Remote Sensing Letters*, vol. 13, no. 1, pp. 8–12, 2016.
- X. Li, Y. He, F. Fioranelli, X. Jing, A. Yarovoy, and Y. Yang, "Human motion recognition with limited radar micro-doppler signatures," *IEEE*

*Transactions on Geoscience and Remote Sensing*, vol. 59, no. 8, pp. 6586–6599, 2021.

[12] J. Wang, R. Li, Y. He, and Y. Yang, “Prior-guided deep interference mitigation for fmcw radars,” *IEEE Transactions on Geoscience and Remote Sensing*, vol. 60, pp. 1–16, 2022.

[13] C. Yu, Z. Xu, K. Yan, Y.-R. Chien, S.-H. Fang, and H.-C. Wu, “Noninvasive human activity recognition using millimeter-wave radar,” *IEEE Systems Journal*, vol. 16, no. 2, pp. 3036–3047, 2022.

[14] L. Werthen-Brabants, G. Bhavanasi, I. Couckuyt, T. Dhaene, and D. Deschrijver, “Quantifying uncertainty in real time with split birnn for radar human activity recognition,” in *2022 19th European Radar Conference (EuRAD)*, 2022, pp. 173–176.

[15] E. Kurtoglu, A. C. Gurbuz, E. A. Malaia, D. Griffin, C. Crawford, and S. Z. Gurbuz, “Asl trigger recognition in mixed activity/signing sequences for rf sensor-based user interfaces,” *IEEE Transactions on Human-Machine Systems*, vol. 52, no. 4, pp. 699–712, 2022.

[16] J. Zhu, H. Chen, and W. Ye, “A hybrid cnn-lstm network for the classification of human activities based on micro-doppler radar,” *IEEE Access*, vol. 8, pp. 24 713–24 720, 2020.

[17] S. Zhu, R. G. Guendel, A. Yarovoy, and F. Fioranelli, “Continuous human activity recognition with distributed radar sensor networks and cnn-rnn architectures,” *IEEE Transactions on Geoscience and Remote Sensing*, vol. 60, pp. 1–15, 2022.

[18] L. Zhu, B. Liao, Q. Zhang, X. Wang, W. Liu, and X. Wang, “Vision mamba: Efficient visual representation learning with bidirectional state space model,” 2024. [Online]. Available: <https://arxiv.org/abs/2401.09417>

[19] M. Ding, G. Dongye, P. Lv, and Y. Ding, “Fml-vit: A lightweight vision transformer algorithm for human activity recognition using fmcw radar,” *IEEE Sensors Journal*, vol. 24, no. 22, pp. 38 518–38 526, 2024.

[20] Y. Zhao, R. G. Guendel, A. Yarovoy, and F. Fioranelli, “Distributed radar-based human activity recognition using vision transformer and cnns,” in *2021 18th European Radar Conference (EuRAD)*, 2022, pp. 301–304.

[21] A. Dosovitskiy, L. Beyer, A. Kolesnikov, D. Weissenborn, X. Zhai, T. Unterthiner, M. Dehghani, M. Minderer, G. Heigold, S. Gelly, J. Uszkoreit, and N. Houlsby, “An image is worth 16x16 words: Transformers for image recognition at scale,” in *International Conference on Learning Representations*, 2021. [Online]. Available: <https://openreview.net/forum?id=YicbFdNTTy>

[22] F. Luo, A. Li, B. Jiang, S. Khan, K. Wu, and L. Wang, “Activitymamba: a cnn-mamba hybrid neural network for efficient human activity recognition,” *IEEE Transactions on Mobile Computing*, pp. 1–15, 2025.

[23] H. Ren, Y. Zhou, J. Zhu, X. Lin, H. Fu, Y. Huang, Y. Fang, F. Ma, H. Yu, and B. Cheng, “Rethinking efficient and effective point-based networks for event camera classification and regression,” *IEEE Transactions on Pattern Analysis and Machine Intelligence*, pp. 1–14, 2025.

[24] M. Linardakis, I. Varlamis, and G. T. Papadopoulos, “Survey on hand gesture recognition from visual input,” 2025. [Online]. Available: <https://arxiv.org/abs/2501.11992>

[25] M. Chakraborty, H. C. Kumawat, S. V. Dhavale, and A. B. Raj A., “Diat-radhnnet: A lightweight dnn for radar based classification of human suspicious activities,” *IEEE Transactions on Instrumentation and Measurement*, vol. 71, pp. 1–10, 2022.

[26] S. Z. Gurbuz, M. M. Rahman, E. Kurtoglu, T. Macks, and F. Fioranelli, “Cross-frequency training with adversarial learning for radar micro-Doppler signature classification (Rising Researcher),” in *Radar Sensor Technology XXIV*, K. I. Ranney and A. M. Raynal, Eds., vol. 11408, International Society for Optics and Photonics. SPIE, 2020, p. 114080A. [Online]. Available: <https://doi.org/10.1117/12.2559155>

[27] A. Shrestha, H. Li, J. Le Kernec, and F. Fioranelli, “Continuous human activity classification from fmcw radar with bi-lstm networks,” *IEEE Sensors Journal*, vol. 20, no. 22, pp. 13 607–13 619, 2020.

[28] S.-w. Kang, M.-h. Jang, and S. Lee, “Identification of human motion using radar sensor in an indoor environment,” *Sensors*, vol. 21, no. 7, 2021. [Online]. Available: <https://www.mdpi.com/1424-8220/21/7/2305>

[29] S. Hochreiter and J. Schmidhuber, “Long short-term memory,” *Neural Computation*, vol. 9, no. 8, pp. 1735–1780, 1997.

[30] J. Chung, C. Gulcehre, K. Cho, and Y. Bengio, “Empirical evaluation of gated recurrent neural networks on sequence modeling,” 2014. [Online]. Available: <https://arxiv.org/abs/1412.3555>

[31] Wikipedia contributors, “American sign language,” [https://en.wikipedia.org/wiki/American\\_Sign\\_Language](https://en.wikipedia.org/wiki/American_Sign_Language), 2025, accessed on April 6, 2025.

[32] L. Tang, Y. Jia, Y. Qian, S. Yi, and P. Yuan, “Human activity recognition based on mixed cnn with radar multi-spectrogram,” *IEEE Sensors Journal*, vol. 21, no. 22, pp. 25 950–25 962, 2021.

[33] H. Sha, W. Zhaoyue, W. Xiaoqiang, W. Limei, Y. Xiaoxuan, H. Hongming, and D. Gan E, “A lightweight hybrid vision transformer network for radar-based human activity recognition,” in *Sci Rep 13*, 2023, p. 17996.

[34] J. Ho, A. Jain, and P. Abbeel, “Denoising diffusion probabilistic models,” 2020. [Online]. Available: <https://arxiv.org/abs/2006.11239>

[35] K. He, X. Zhang, S. Ren, and J. Sun, “Deep residual learning for image recognition,” 2015. [Online]. Available: <https://arxiv.org/abs/1512.03385>

[36] D. P. Kingma and J. Ba, “Adam: A method for stochastic optimization,” *arXiv preprint arXiv:1412.6980*, 2014.

[37] I. Loshchilov and F. Hutter, “Decoupled weight decay regularization,” in *International Conference on Learning Representations*, 2019. [Online]. Available: <https://openreview.net/forum?id=Bkg6RiCqY7>

[38] M. Horowitz, “1.1 computing’s energy problem (and what we can do about it),” in *2014 IEEE international solid-state circuits conference digest of technical papers (ISSCC)*. IEEE, 2014, pp. 10–14.



**Yizhuo Wu** (Student Member, IEEE) obtained her M.Sc. degree in Microelectronics at TU Delft in 2023. She is now a PhD student supervised by Dr. Chang Gao in the Lab of Efficient Machine Intelligence (EMI). Her research focuses on software-hardware co-designed AI for I/Q signal processing, which aims to find energy-efficient solutions for high-frequency signal processing tasks.



**Francesco Fioranelli** (Senior Member, IEEE) received the Laurea (B.Eng., cum laude) and Laurea Specialistica (M.Eng., cum laude) degrees in telecommunication engineering from the Università Politecnica delle Marche, Ancona, Italy, in 2007 and 2010, respectively, and the Ph.D. degree from Durham University, U.K., in 2014. He is currently an Associate Professor with TU Delft, Delft, The Netherlands. He was a Research Associate at University College London, London, U.K., from 2014 to 2016, and an Assistant Professor at the University of Glasgow, Glasgow, U.K., from 2016 to 2019. He has authored over 190 peer-reviewed publications and edited the books titled Micro-Doppler Radar and Its Applications and Radar Countermeasures for Unmanned Aerial Vehicles published by IET-Scitech in 2020. His research interests include the development of radar systems and automatic classification for human signatures analysis in healthcare and security, drone and UAV detection and classification, automotive radar, wind farms, and sea clutter. Dr. Fioranelli received four best paper awards and the IEEE AEES Fred Nathanson Memorial Radar Award in 2024.



**Chang Gao** (Member, IEEE) received his Ph.D. degree with distinction in Neuroscience from the Institute of Neuroinformatics, University of Zürich and ETH Zürich, Zürich, Switzerland, in March 2022. He received his M.Sc. degree from Imperial College London in September 2016 and his B.Eng. degree from the University of Liverpool and Xi'an Jiaotong-Liverpool University in July 2015. In August 2022, he joined Delft University of Technology, The Netherlands, as a tenured Assistant Professor in the Department of Microelectronics. He leads the Lab of Efficient Machine Intelligence (EMI), where he conducts research on hardware-software co-design for edge AI computing and embodied intelligence. He received the 2022 Misha Mahowald Early Career Award in Neuromorphic Engineering and a 2022 Marie Skłodowska-Curie Postdoctoral Fellowship. He is a 2023 Dutch Research Council (NWO) Veni laureate and a 2023 MIT Technology Review Innovator Under 35 in Europe for his contributions to algorithm-hardware co-design for efficient sparse recurrent neural-network edge computing.